

Spectrally resolved bioluminescence tomography with adaptive finite element analysis: methodology and simulation

Yujie Lv¹, Jie Tian^{1,2}, Wenxiang Cong³, Ge Wang³, Wei Yang¹,
Chenghu Qin¹ and Min Xu¹

¹ Medical Image Processing Group, Institute of Automation, Chinese Academy of Sciences,
PO Box 2728, Beijing 100080, People's Republic of China

² Life Science Center, Xidian University, Xian, Shaanxi 710071, People's Republic of China

³ Division of Biomedical Imaging, VT-WFU School of Biomedical Engineering and Sciences,
Virginia Polytechnic Institute and State University, Blacksburg, VA 24061, USA

E-mail: tian@ieee.org and ge-wang@ieee.org

Received 12 February 2007, in final form 18 April 2007

Published 3 July 2007

Online at stacks.iop.org/PMB/52/4497

Abstract

As a molecular imaging technique, bioluminescence tomography (BLT) with its highly sensitive detection and facile operation can significantly reveal molecular and cellular information *in vivo* at the whole-body small animal level. However, because of complex photon transportation in biological tissue and boundary detection data with high noise, bioluminescent sources in deeper positions generally cannot be localized. In our previous work, we used achromatic or monochromatic measurements and an *a priori* permissible source region strategy to develop a multilevel adaptive finite-element algorithm. In this paper, we propose a spectrally solved tomographic algorithm with *a posteriori* permissible source region selection. Multispectral measurements, and anatomical and optical information first deal with the nonuniqueness of BLT and constrain the possible solution of source reconstruction. The use of adaptive mesh refinement and permissible source region based on *a posteriori* measures not only avoids the dimension disaster arising from the multispectral measured data but also reduces the ill-posedness of BLT and therefore improves the reconstruction quality. Reconsideration of the optimization method and related modifications further enhance reconstruction robustness and efficiency. We also incorporate into the method some improvements for reducing computational burdens. Finally, using a whole-body virtual mouse phantom, we demonstrate the capability of the proposed BLT algorithm to reconstruct accurately bioluminescent sources in deeper positions. In terms of optical property errors and two sources of discernment in deeper positions, this BLT algorithm represents the unique predominance for BLT reconstruction.

(Some figures in this article are in colour only in the electronic version)

1. Introduction

Because of its unique characteristic as a small animal molecular imaging modality, bioluminescence imaging has rapidly developed in recent years. Compared with nuclear imaging, bioluminescence imaging has an indispensable position in biological study (Contag and Bachmann 2002, Bhaumik and Gambhir 2002, Massoud and Gambhir 2003). However, tomographically observing the molecular and cellular activities at the whole-body small animal level, that is, bioluminescence tomography (BLT) (Wang *et al* 2003), still faces challenging problems. Theoretically, three-dimensional reconstruction of bioluminescent sources is an inverse source problem that has not been greatly investigated. In highly heterogeneous biological tissues, scattering and absorption of the photon emitted by a bioluminescent source increases the difficulty of source localization. In addition, although the absence of external illumination accords a highly sensitive signal, it complicates the tomographic problem. Therefore, the unique and accurate reconstruction of bioluminescent sources and the development of a fast and robust tomographic algorithm are topics for further investigation (Ntziachristos *et al* 2005).

Based on diffusion approximation theory, the uniqueness theorem shows that the BLT solution generally is not unique (Wang *et al* 2004). It is necessary to incorporate *a priori* information for accurate BLT reconstruction. Taking into account the surface light power distribution and the heterogeneous structure of the phantom, the BLT reconstruction method employing *a priori* permissible source region was developed (Cong *et al* 2004, 2005b, Lv *et al* 2006). However, it is not always reliable to infer such a permissible region especially when deeper and/or multiple bioluminescent sources exist in a small animal. In view of the spectral characteristics of the underlying bioluminescent sources, hyper- and multi-spectral BLT methods were also proposed (Kuo *et al* 2004, Chaudhari *et al* 2005, Alexandrakis *et al* 2005, Cong and Wang 2006, Dehghani *et al* 2006). Note that the assumption of a homogeneous optical background is inadequate for the spectrally resolved bioluminescence tomography, especially for deeper bioluminescent source reconstruction in the small animal (Alexandrakis *et al* 2005).

An algorithm that allows for fast and robust BLT imaging is essential for practical application to biological research. Since scattering predominates absorption in most biological tissues, the diffusion approximation model has been successfully applied in bio-photonics (Gibson *et al* 2005). Recently, the analytical method suitable for complex boundaries (Ripoll *et al* 2002) and numerical acceleration algorithms (Ye *et al* 2001, Joshi *et al* 2004) improved the computational speed of inversion schemes in fluorescence imaging. As for BLT, the multilevel adaptive finite-element algorithm was developed using achromatic or monochromatic measurements and *a priori* permissible source region which improved the reconstruction quality and speed (Lv *et al* 2006). However, with the introduction of spectral information and the development of the noncontact detection mode (Ripoll *et al* 2003), the large-scale data set seriously affects source reconstruction speed despite the fact that it increases the acquisition of valid information. Using the depth-dependent spectral space transformation, the dimension of the boundary measured data is greatly reduced and promising reconstruction results are obtained (Chaudhari *et al* 2005).

In this paper, a novel tomographic algorithm employing an adaptive finite-element method and spectrally resolved measurement is proposed for BLT reconstruction. The most distinct difference between the current and previous algorithms is the development of an *a posteriori* permissible source region strategy. Based on a diffusion approximation model, this algorithm considers the heterogeneous characteristics of a small animal as well as the spectral information of the bioluminescent sources as *a priori* information which adequately

deals with the nonuniqueness of BLT. The combination of *a posteriori* permissible region selection and adaptive mesh evolution not only improves the reconstruction quality and reduces the ill-posedness of BLT, but also avoids the dimensional disaster arising from using the spectrally resolved data. The spectral projected gradient-based optimization and related modifications improve reconstruction efficiency and robustness. Some improvements for reducing computational burden are also fused into the proposed algorithm. In the numerical reconstruction, a micro-MRI-based real mouse image is employed to provide the anatomical information (Segars *et al* 2004), and the optical properties corresponding to the segmented tissues also are determined through *a priori* experimental results (Alexandrakis *et al* 2005). Using the multiple-material marching-cubes algorithm (M3C) (Wu and Sullivan 2003), the surface and volumetric meshes of the whole-body mouse are established at different scale levels, which provide a series of standard models for simulation and reconstruction. In order to acquire the measured data, multispectral data are generated through a modified molecular optical simulation environment (MOSE) that we developed based on Monte Carlo simulation. A series of bioluminescent source reconstructions shows the merits and potentials of the proposed tomographic algorithm for practical BLT reconstruction.

The paper is organized as follows. The next section introduces the proposed BLT algorithm that incorporates spectral information and adaptive finite-element analysis. Experimental setups, such as disposal of the small mouse phantom, acquisition of the synthetic data and so on, are also demonstrated in the second section. A series of BLT reconstructions is described in section 3. Finally, a discussion of relevant issues and a conclusion are provided.

2. Methods

2.1. Diffusion approximation

At present, the reported luciferase enzymes may realize bioluminescent reporters (Zhao *et al* 2005). When a bioluminescence imaging experiment is performed in a dark environment, the propagation of photons in biological tissues can be suitably modeled by a steady-state diffusion equation and Robin boundary condition (Cong *et al* 2005b, Chaudhari *et al* 2005). If the influence of light wavelength λ on tissue optical properties is considered, the following models are given:

$$-\nabla \cdot (D(\mathbf{x}, \lambda) \nabla \Phi(\mathbf{x}, \lambda)) + \mu_a(\mathbf{x}, \lambda) \Phi(\mathbf{x}, \lambda) = S(\mathbf{x}, \lambda) \quad (\mathbf{x} \in \Omega) \quad (1)$$

$$\Phi(\mathbf{x}, \lambda) + 2A(\mathbf{x}; n, n') D(\mathbf{x}, \lambda) (\mathbf{v}(\mathbf{x}) \cdot \nabla \Phi(\mathbf{x}, \lambda)) = 0 \quad (\mathbf{x} \in \partial\Omega) \quad (2)$$

where Ω and $\partial\Omega$ are the domain and the corresponding boundary; $\Phi(\mathbf{x}, \lambda)$ denotes the photon flux density (W mm^{-2}); $S(\mathbf{x}, \lambda)$ is the source energy density (W mm^{-3}); $\mu_a(\mathbf{x}, \lambda)$ is the absorption coefficient (mm^{-1}); $D(\mathbf{x}, \lambda) = 1/(3(\mu_a(\mathbf{x}, \lambda) + (1 - g)\mu_s(\mathbf{x}, \lambda)))$ is the optical diffusion coefficient, $\mu_s(\mathbf{x}, \lambda)$ is the scattering coefficient (mm^{-1}), and g is the anisotropy parameter; \mathbf{v} is the unit outer normal on $\partial\Omega$. In the practical experiment, if the outgoing flux density is detected with a bandpass filter, the continuous spectral range of bioluminescent reporters is divided into several bands $wb_k \in [\lambda_k, \lambda_{k+1}]$, $k = 1, 2, \dots, K$.

2.2. Algorithm

The following mathematical notations demonstrate the proposed algorithm. In adaptive finite-element analysis, a sequence $\{\mathcal{T}_1, \dots, \mathcal{T}_l, \dots\}$ of nested triangulations to the given domain Ω can be generated by local mesh refinement. $N_{\mathcal{T}_l}$ elements and $N_{\mathcal{P}_l}$ vertex nodes exist in each triangulation \mathcal{T}_l . A sequence $\{\mathcal{V}_1, \dots, \mathcal{V}_l, \dots\}$ of finite-element spaces also corresponds to the

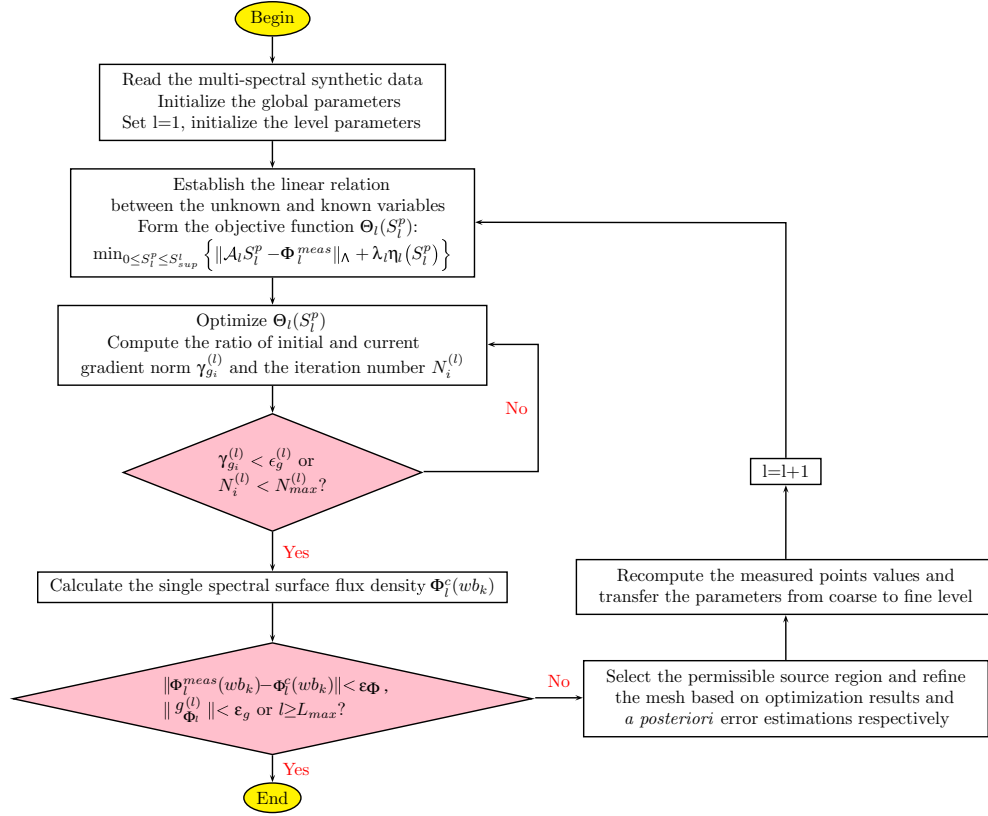


Figure 1. The flowchart of the proposed BLT tomographic algorithm.

nested triangulations. Figure 1 shows the flow of the proposed algorithm. Some steps have been thoroughly explained in a previous publication (Lv et al 2006). A focused discussion of the proposed algorithm will explain the differences. As a whole, three main changes are developed for the spectrally resolved BLT algorithm, including a *a posteriori* permissible source region selection, reconsideration of the optimization method and related modifications, and some improvements for reducing computational burden.

Establish the linear relationship between unknown and known variables. In view of multispectral measurement, a direct relationship between boundary measurable photon density and unknown bioluminescent source distribution is established using an *a posteriori* permissible source region strategy which is distinctly different from our previous algorithm. Now, only one single-band wb_k is considered. On the \mathcal{T}_l triangulation to the given domain, we can obtain the matrix form of equations (1) and (2) using the finite-element method that follows (Lv et al 2006):

$$(K_l(wb_k) + C_l(wb_k) + B_l(wb_k))\Phi_l(wb_k) = F_l(wb_k)S_l(wb_k). \quad (3)$$

Let $M_l(wb_k) = K_l(wb_k) + C_l(wb_k) + B_l(wb_k)$, where $M_l(wb_k)$ is a symmetric positive-definite matrix. Considering the linear relationship between the unknown source variable $S_l(wb_k)$ and the boundary measured flux density $\Phi_l^{\text{meas}}(wb_k)$, we have

$$\Phi_l^{\text{meas}}(wb_k) = G_l(wb_k)S_l(wb_k) \quad (4)$$

where $\mathcal{G}_l(wb_k)$ can be established by removing those rows of $[M_l(wb_k)^{-1}F_l(wb_k)]$ corresponding to the nonmeasurable points. Furthermore, the energy percentage of each spectral band wb_k can be determined beforehand by the experimental spectral analysis of the bioluminescent sources, that is $S(wb_k) = \omega(wb_k)S$, where $\omega(wb_k) \geq 0$ and $\sum_{k=1}^K \omega(wb_k) \approx 1$, S denotes total photon density. Taking into account the above spectral distribution and the selection of permissible source region, we have

$$\Phi_l^{\text{meas}} = \mathcal{G}_l \mathcal{W}_l^S S_l \quad (5)$$

where

$$\Phi_l^{\text{meas}} = \begin{bmatrix} \Phi_l^{\text{meas}}(wb_1) \\ \Phi_l^{\text{meas}}(wb_2) \\ \vdots \\ \Phi_l^{\text{meas}}(wb_K) \end{bmatrix}, \quad \mathcal{G}_l = \begin{bmatrix} \omega(wb_1)\mathcal{G}_l(wb_1) \\ \omega(wb_2)\mathcal{G}_l(wb_2) \\ \vdots \\ \omega(wb_K)\mathcal{G}_l(wb_K) \end{bmatrix}. \quad (6)$$

\mathcal{W}_l^S is a diagonal matrix for selecting the permissible source region, that is

$$\begin{aligned} \mathcal{W}_l^S &= \text{Diag}(w_{l(11)}^S, w_{l(22)}^S, \dots, w_{l(ii)}^S, \dots, w_{l(N_{P_l}N_{P_l})}^S), \\ w_{l(ii)}^S &= \begin{cases} 0 & \{s'_{l(ii)} < \gamma_{sp}^{(l)} s'_{l(i)}^{\max}, l > 1\} \\ 1 & \{l = 1\} \text{ or } \{s'_{l(ii)} \geq \gamma_{sp}^{(l)} s'_{l(i)}^{\max}, l > 1\}. \end{cases} \end{aligned} \quad (7)$$

$s'_{l(i)}$ and $s'_{l(i)}^{\max}$ are the reconstructed results prolonged from the $(l-1)$ th level and the corresponding maximum, that is

$$S'_l = I_{l-1}^l S'_{l-1} \quad (l \geq 2). \quad (8)$$

I_{l-1}^l is the prolongation operator, $\gamma_{sp}^{(l)}$ is the ratio factor, and S'_{l-1} is the reconstructed results on the $(l-1)$ th level. By retaining those columns of $\mathcal{G}_l \mathcal{W}_l^S$ corresponding to the permissible source region S_l^p , the following linear system is obtained:

$$\mathcal{A}_l S_l^p = \Phi_l^{\text{meas}}. \quad (9)$$

Form the objective function and select effective optimization method. Because \mathcal{A}_l is a severely ill-conditioned matrix because of the ill-posedness of BLT, the surface measured data with noise will lead to failure in solving equation (9) directly (Hansen 1999). For the medium- and large-scale problems, iterative methods are suitable for only the matrix–vector computational requirement (Hanke and Hansen 1993). Nonetheless, iterative methods sometimes suffer from slow convergence and instability because of the ill-posed nature. It is necessary to add *a priori* information-based constraints into the problem. Iterative methods are not better at dealing with the beneficial information. In optical tomographic imaging, with respect to the physical meaning of variable parameters, dealing with a constrained minimization problem using optimization methods has an important impact on object reconstruction (Roy and Sevik-Muraca 2000). In BLT, the source density constraint may be used as *a priori* information. Therefore, the following l th minimization $\Theta_l(S_l^p)$ is defined with Tikhonov regularization methods:

$$\min_{0 \leq S_l^p \leq S_l^{\text{sup}}} \Theta_l(S_l^p) = \{\|\mathcal{A}_l S_l^p - \Phi_l^{\text{meas}}\|_{\Lambda} + \lambda_l \eta_l(S_l^p)\} \quad (10)$$

where S_l^{sup} is the l th level upper bound of source density; Λ is the weight matrix, $\|V\|_{\Lambda} = V^T \Lambda V$; λ_l the regularization parameter; and $\eta_l(\cdot)$ is the penalty function. For $\Theta_l(S_l^p)$ as a least-squares problem with simple bounds, numerical experiments indicate that

the efficiency of the algorithm depends largely on how to better manage bound constraints, especially in large-scale optimization problems (Diniz-Ehrhardt *et al* 1997). Therefore, the spectral projected gradient-based large-scale optimization algorithm is modified to solve the above problem (Birgin and Martinez 2002). In addition, the multilevel characteristic improves numerical stability and accelerates the convergence speed of this optimization procedure (Lv *et al* 2006).

Triggered conditions of mesh refinement and convergence criterion. Although different objective functions must be treated because of adaptive mesh evolution and a *posteriori* permissible source region selection, a final reasonable solution needs to be found which makes the gradient norm $\|g_{\Theta_l}(S_l^p)\|$ approach 0, where $g_{\Theta_l}(S_l^p) = \nabla \Theta_l(S_l^p)$. Using the selected optimization method, we modify related measure criteria. The norm ratio $\gamma_{g_i}^{(l)}$ of the current gradient $g_{\Theta_l}^i$ to the initial one $g_{\Theta_l}^0$ and the iteration number $N_i^{(l)}$ on each level are selected as switch indexes. As for the stopping criterion, we use the current gradient norm $\|g_{\Phi_l}^{(l)}\|$ on the l th level, the number l of mesh refinements, or the discrepancy between the measured and computational boundary nodal flux data to evaluate if the whole procedure should be terminated. The boundary flux density on one single band is calculated to reduce computational burden.

Error estimation and local mesh refinement. A *posteriori* error estimation and local mesh refinement have been thoroughly explained in Lv *et al* (2006). Although an *a posteriori* permissible source region strategy is proposed in this algorithm, similar disposal methods can be used after the permissible and forbidden source regions are selected on the l th discretized level. Note that the computational error distribution on different spectral bands are consistent with each other because the same diffusion approximation and discretized domain are used even though their discrepancy is used to improve BLT reconstruction. The error estimation on a single spectral band is performed in the forbidden source region in order to reduce the computational burden.

2.3. Materials

Various phantoms have been designed for near-infrared (NIR) imaging studies. However, different geometries of phantoms lead to different results for the same reconstruction object because of the ill-posedness of the problem (Pogue *et al* 1999). In order to optimally establish and evaluate the tomographic algorithm, it is preferable to choose the phantom which approaches the final applied geometry. For finite-element-based BLT reconstruction, the volumetric mesh of the whole-body small animal is necessary. During its generation, the popular single-material marching-cubes (SMMC) algorithm and its variations are not suitable for heterogeneity consideration (Lorensen and Cline 1987). Recently, the multiple-material marching-cubes (M3C) algorithm (Wu and Sullivan 2003) and multiregional marching-tetrahedra (MMT) method (Cong *et al* 2005a) have been developed to deal with the multimaterial domains. In this study, a microMRI-based whole-body mouse volume (MOBY) was used to evaluate the proposed algorithm (Segars *et al* 2004). The M3C algorithm with modified surface mesh smooth and simplification methods, as well as the advancing front technique, generated different scale meshes of the whole-body mouse phantom (Wu 2001). One of them is shown in figure 2. In the following experiments, for nonscattering regions of the mouse brain, only the mouse torso, from the neck to the base of the tail, was used. Its initial coarse volumetric finite-element mesh included 725 nodes and 3548 tetrahedral elements.

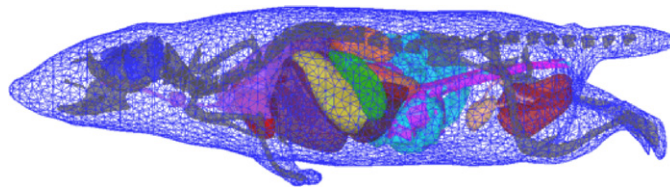


Figure 2. The view of the MOBY mouse phantom.

Table 1. Optical properties of biological tissues in mouse in different wavelength ranges.

Bands	500–550 nm		550–600 nm		600–650 nm		650–700 nm		700–750 nm	
	μ_a^a	$\mu_s'^a$	μ_a	μ_s'	μ_a	μ_s'	μ_a	μ_s'	μ_a	μ_s'
Bone	9.0×10^{-3}	3.34	2.2×10^{-3}	2.93	6.0×10^{-4}	2.61	3.6×10^{-4}	2.34	5.9×10^{-4}	2.11
Fat	6.2×10^{-4}	1.34	2.5×10^{-4}	1.28	2.1×10^{-4}	1.22	3.4×10^{-4}	1.18	1.2×10^{-3}	1.14
Heart	9.1×10^{-3}	1.28	2.2×10^{-3}	1.13	6.9×10^{-4}	1.00	5.8×10^{-4}	0.91	1.4×10^{-3}	0.82
Intestine	1.7×10^{-3}	1.47	5.3×10^{-4}	1.32	2.8×10^{-4}	1.19	3.8×10^{-4}	1.09	1.3×10^{-3}	0.99
Kidney	1.0×10^{-2}	3.04	2.6×10^{-3}	2.66	8.6×10^{-4}	2.36	8.0×10^{-4}	2.11	2.2×10^{-3}	1.90
Liver	5.4×10^{-2}	0.83	1.2×10^{-2}	0.76	3.4×10^{-3}	0.70	2.0×10^{-3}	0.65	3.0×10^{-3}	0.60
Lung	2.7×10^{-2}	2.41	7.1×10^{-3}	2.30	2.0×10^{-3}	2.21	1.4×10^{-3}	2.12	2.8×10^{-3}	2.04
Pancreas	1.0×10^{-2}	3.04	2.6×10^{-3}	2.66	8.6×10^{-4}	2.36	8.0×10^{-4}	2.11	2.2×10^{-3}	1.90
Spleen	5.4×10^{-2}	0.83	1.3×10^{-2}	0.76	3.4×10^{-3}	0.70	2.0×10^{-3}	0.65	3.0×10^{-3}	0.60
Stomach	1.8×10^{-3}	1.74	6.0×10^{-4}	1.60	3.8×10^{-4}	1.48	5.7×10^{-4}	1.38	2.0×10^{-3}	1.29

^a Unit: mm^{-1} .

Many publications have reported the respective measurement results for optical properties of biological tissues. For data sparsity and incompleteness, the reported tissue optical properties are compiled in the literature (Alexandrakis *et al* 2005). The absorption (μ_a) and reduced scattering (μ_s') coefficients assigned to each organ as a function of photon wavelength are estimated on the basis of this compilation. In addition, the main absorbers of near-infrared (NIR) light in biological tissues are oxy-hemoglobin (HbO_2), deoxy-hemoglobin (Hb) and water. Their influence is also applied to estimate absorption coefficients. However, *in vivo* small animal studies bring the difference between individuals in tissue optical properties. The inevitable optical property discrepancy between *in vitro* experimental acquisition and actual physiological values affects the tomographic localization of bioluminescent sources (Alexandrakis *et al* 2006).

In all of the simulation experiments, we assumed that the observed PC3M-Luc cells were tagged with firefly luciferase, and the cells emitted bioluminescent photons in the spectral range [500 nm, 750 nm] (Coquoz *et al* 2003). According to current measurement technology, we could divide the whole emission spectrum into five regions with discrete steps of 50 nm (Dehghani *et al* 2006). Note that the proposed tomographic algorithm is suitable for other bioluminescent reporters and tagged targets through the prior measurement of the emission spectral characteristics even though the specified reporter and target are used here. The organs defined by MOBY in the mouse torso were further dealt with because information about their optical properties was absent from current literature data, which were the same with those in Alexandrakis *et al* (2005). Detailed information about optical properties of biological tissues is presented in table 1.

For performance evaluation of the BLT algorithms, the Monte Carlo (MC) method is considered to synthesize the measured data in view of its precision and *inverse crime* problem

(Lv *et al* 2006). A modification to the MOSE platform that we have developed (Li *et al* 2004) was performed, which made the MOSE platform suitable for multispectral simulation. This platform used the surface mesh of the mouse phantom with about 14 600 triangle facets to generate the synthetic data. In the simulation, each spectral region of bioluminescent source was sampled by 1.0×10^6 photons.

In the following experiments, a spherical source with 1.0 mm radius and 1.0 nW total power was used for verifications. In addition, the upper bound S_{sup}^l , the weighted matrix Λ and the penalty function $\eta_l(X) = X^T X$ were identical with those in Lv *et al* (2006). The gradient ratio tolerance $\epsilon_g^{(l)}$ and the maximum iteration number $N_{\text{max}}^{(l)}$ were invariable at each level, being equal to 1.0×10^{-5} and 5000, respectively. The terminated gradient norm ϵ_g , the stopping threshold ϵ_Φ , and the maximum number of mesh refinements L_{max} were set to 7.0×10^{-9} , 1.0×10^{-7} and 3, respectively. At the coarsest mesh level, the whole reconstruction object was the permissible source region. After mesh refinement, the ratio factor $\gamma_{sp}^{(l)}$ was initially set to 10^{-4} for selecting the permissible source region. With the increase in l , the factor was changed by multiplying a factor of 10.0. The same elements refinement ratio as that in Lv *et al* (2006) was used here. The reconstruction procedure began with an initial guess $S_{\text{init}}^{(1)}$ of 1.0×10^{-6} . All reconstructions were implemented on a PC with an Intel processor (Pentium 4 2.8 GHz) and 1 GB of RAM.

3. Results

3.1. Single versus multiple spectral reconstruction in different depths

The achromatic or monochromatic measurement-based tomographic algorithm cannot achieve desirable results for deeper source reconstruction (Alexandrakis *et al* 2005). When the bioluminescent source was located at half-radius position from the mouse surface, we selected

$$P_s = \{(x, y, z) | 2 \leq x \leq 32, 17 \leq y \leq 32, 28 \leq z \leq 34, (x, y, z) \in \text{mouse phantom}\}$$

as the permissible source region through the light power distribution on the mouse surface. Using the monochromatic synthetic data in [600 nm, 650 nm], the corresponding reconstructed results are shown in figure 3(a) based on our previous algorithm (Lv *et al* 2006). Despite the fact that the *a priori* permissible source region strategy was utilized, the BLT reconstruction became undesirable because of the deep position of the reconstructed source. Furthermore, using the proposed algorithm and monochromatic measurement, BLT reconstructions were performed when the sources were placed at half-radius and center positions. Figures 3(b) and (c) demonstrate the reconstructed results via two mesh evolutions. With the absence of *a priori* information, BLT reconstruction on a coarse mesh did not roughly localize the source position, leading to imprecise, even inaccurate, localization on a fine mesh.

The multispectral measurement-based BLT reconstruction showed preferable results for sources at half-radius and center positions by the combination of adaptive mesh evolution and *a posteriori* permissible source region selection, as shown in figures 4(a) and (c). Two adaptive mesh refinements were performed in the whole reconstruction procedure, and figure 5 shows the evolution of surface mesh and reconstructed results with the bioluminescent source placed at half-radius position. The corresponding change of the objective function $\Theta_l(S_l^p)$ and the L_2 direction gradient norm $\|g_{\Theta_l}(S_l^p)\|$ are displayed in figures 4(b) and (d). Although the value of the objective function increased as the selection of *a posteriori* permissible source region and adaptive mesh evolution, the norm of the direction gradient always dropped sharply, which was a reasonable response for the whole optimization procedure and BLT reconstruction. From the above comparisons, it is obvious that the proposed algorithm is superior to our previous method,

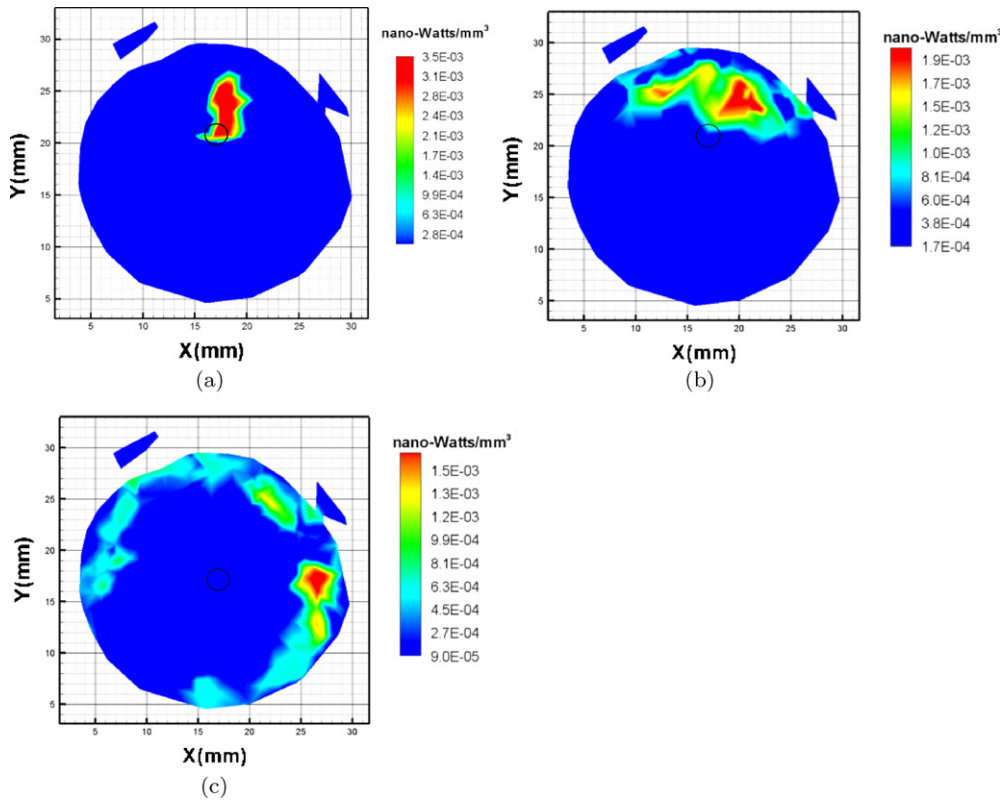


Figure 3. BLT reconstruction with monochromatic synthetic data in [600 nm, 650 nm]. (a) Transverse view of the reconstructed results for a spherical source located at half-radius position in the mouse phantom using the *a priori* permissible source region strategy. Parts (b) and (c) are the counterparts when the sources are respectively located at half-radius and center positions using *a posteriori* permissible source region selection. For the best display, the cross section perpendicular to the *z*-axis direction is about 1 mm off the actual source's center. The black circle represents the actual source position.

especially for reconstructing a deep source. Nevertheless, spectrally resolved measurement is indispensable and provides more sufficient *a priori* information.

3.2. Reconstruction comparisons between fixed versus *a posteriori* selective source spaces

In the domain discretization-based BLT reconstruction, the achievable resolution and the position and shape of the reconstructed source are relevant to the scale of discretization. Generally, when the fine mesh of the phantom is used, we obtain more desirable results in view of the flexibility of small discretized elements. However, the finer the discretized mesh is, the longer the time to reconstruction and the more ill-posed the BLT problem becomes. A possible solution, which can be obtained in certain optimization methods, is not likely to be the physically desirable solution because of the ill-posed nature of BLT. Figure 6 shows the reconstructed results on three different discretized scale meshes when the bioluminescent source was located at half-radius position in the mouse phantom and the same multispectral synthetic data were used. The quantitative information of BLT reconstructions is shown

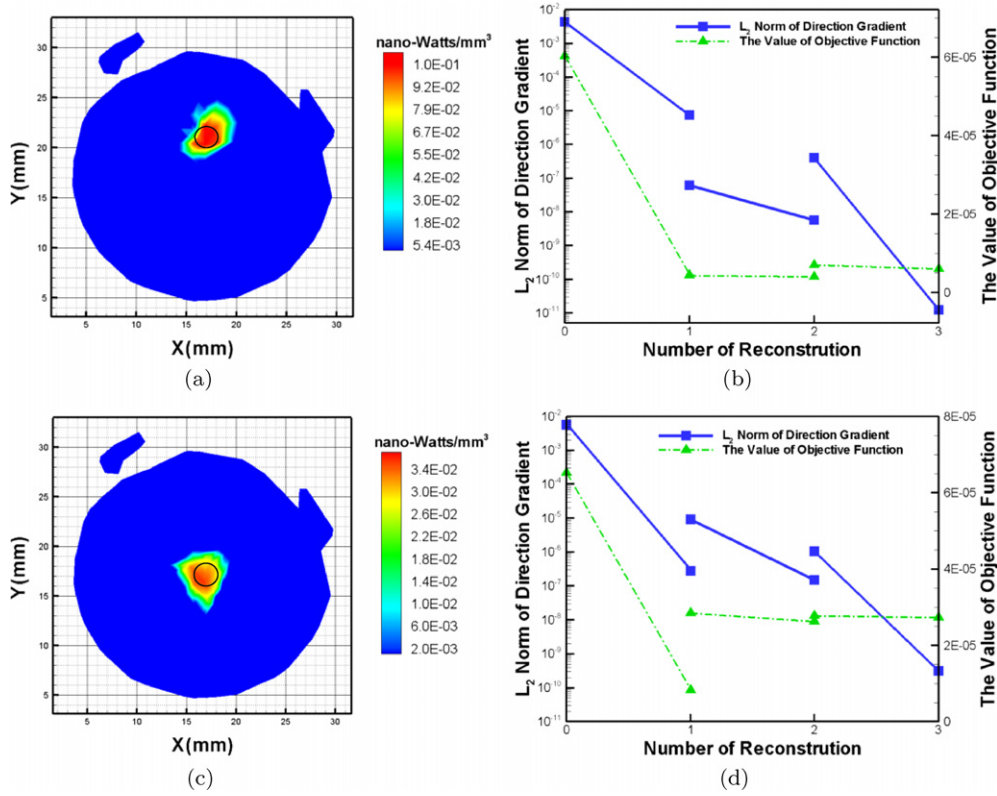


Figure 4. Spectrally resolved BLT reconstruction with the proposed algorithm. (a) and (c) Transverse views of the reconstructed results with actual sources placed at half-radius and center positions in the mouse phantom respectively. The cross section perpendicular to the z -axis direction is through the actual source's center. (b) and (d) Quantitative information of the reconstruction procedure corresponding to (a) and (c). Dashed dot lines denote the value change of objective function $\Theta_l(S_l^p)$ and solid lines denote the L_2 norm change of direction gradient $g_{\Theta_l}(S_l^p)$.

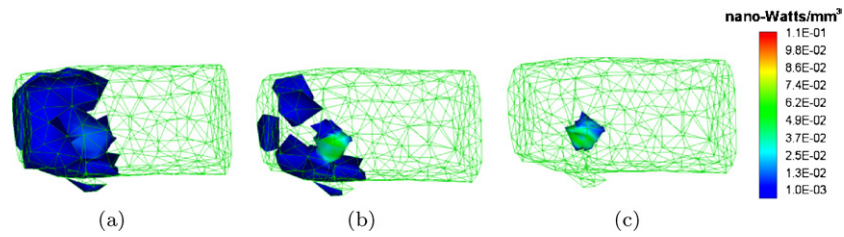


Figure 5. (a), (b) and (c) The evolution of surface mesh and reconstructed results when the source is placed at half-radius position. The mesh denotes the surface mesh of the mouse phantom.

in table 2. Although the time cost gradually decreased with the reduction of the number of elements, surface measured points and optimization variables, the reconstructed results were similarly undesirable through the whole region-based reconstruction and use of *a priori* information. When the reconstruction procedure started from the coarse mesh, with the goal-oriented mesh refinement and *a posteriori* permissible source region selection, desirable

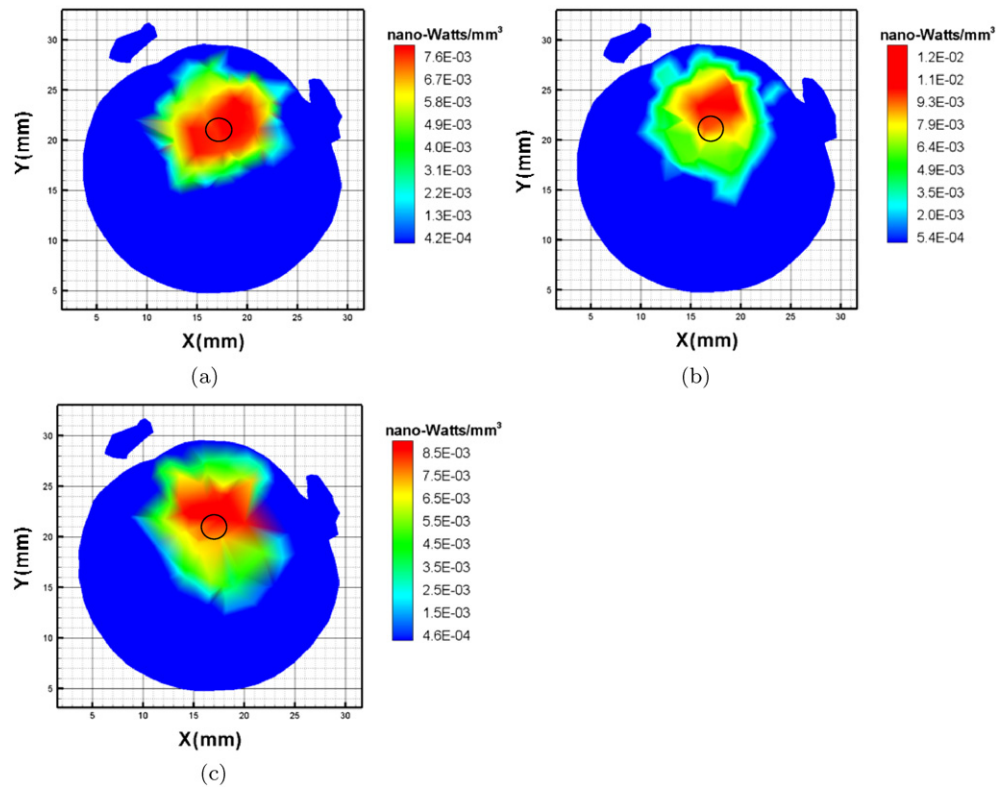


Figure 6. The whole region-based BLT reconstruction without adaptive mesh refinement and *a posteriori* permissible source region selection on the fixed mesh of different discretized scales. The discretized scale becomes gradually coarse from (a) to (c). The cross section is through the actual source's center. Detailed information about the mesh and reconstruction can be found in table 2.

Table 2. Quantitative comparison between the fixed mesh of three different discretized scales and the adaptive evolution mesh. BLT reconstruction was accomplished with a PC with an Intel processor (Pentium 4 2.8 GHz) and 1 GB of RAM.

Cases	Elements	Measured points	Variables	Refinements	Time cost (min.)
Figure 6(a)	25 471	1018	4922	0	107.0
Figure 6(b)	19 472	975	3904	0	66.0
Figure 6(c)	14 109	678	2803	0	22.0
Figure 4(a)	7104	187	110	2	4.0

results were obtained along with a remarkable reduction of time cost, as shown in figure 4(a) and table 2.

3.3. Optical property errors consideration

Optical properties of mouse tissues as *a priori* information are essential for reducing the ill-posedness of BLT and for dealing with the nonuniqueness of BLT (Wang *et al* 2004,

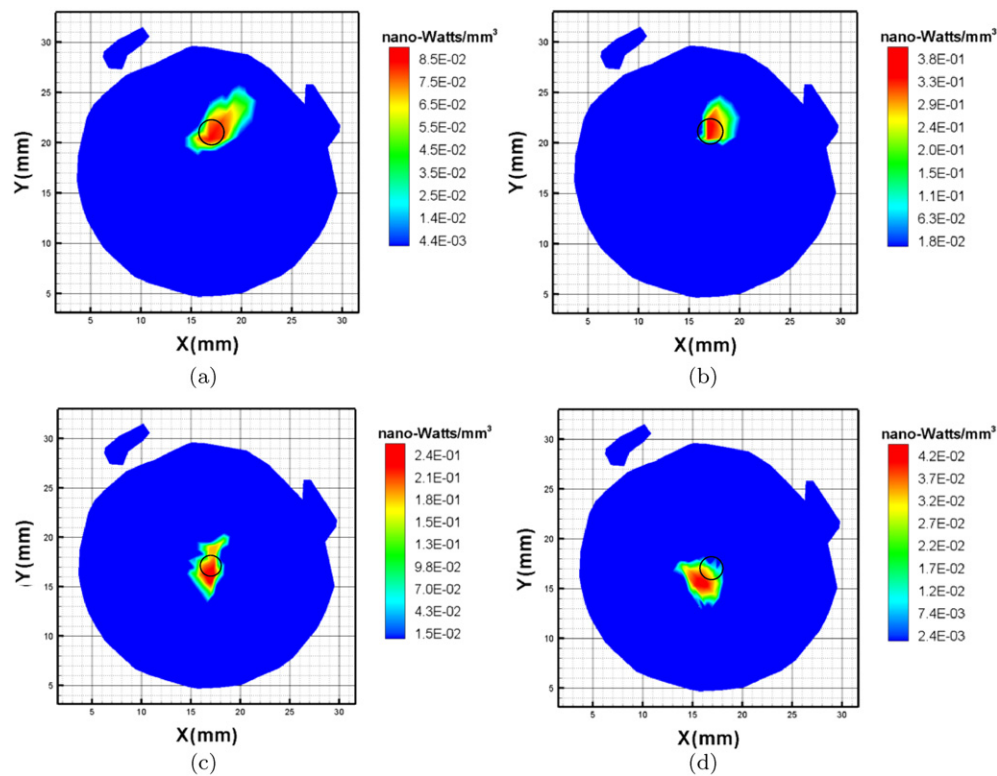


Figure 7. BLT reconstruction with the proposed algorithm in view of optical property errors. Parts (a) and (b) are the reconstructed results corresponding to +50% and −50% optical property errors for all tissues when the bioluminescent source is located at half-radius position in the mouse phantom; (c) and (d) are the counterparts when the source is located at the mouse's center. Two local mesh refinements were implemented in BLT reconstruction. The cross section is through the actual source's center.

Alexandrakis *et al* 2005). The complex tissues of *in vivo* small animals require simultaneous optical property measurements. The diffuse optical tomography (DOT) technique, as a fusion-imaging modality, is appropriate for BLT. Currently, the quantification accuracy of DOT reconstruction can achieve a 10–50% error range depending on various factors (Ntziachristos *et al* 2001). Here, $\pm 50\%$ errors for all tissues were considered for BLT reconstruction. When the bioluminescent source was placed at half-radius position in the mouse phantom, the desirable reconstructed results for the underestimation and overestimation of optical properties were similar with that in figure 4(a) based on normal ones, as shown in figures 7(a) and (b). As the source depth increased, the optical property errors increasingly affected the BLT reconstruction (Alexandrakis *et al* 2006). However, using the proposed tomographic algorithm, the source reconstruction at the mouse's center acquired desirable results when $\pm 50\%$ optical property errors were considered for all tissues, as shown in figures 7(c) and (d). Although the center position of the reconstructed source had the maximum offset of about 1 mm compared with the actual one, the ring-like shape results did not appear in this BLT reconstruction (Alexandrakis *et al* 2006) which presented the algorithm's capability for tolerating optical property errors.

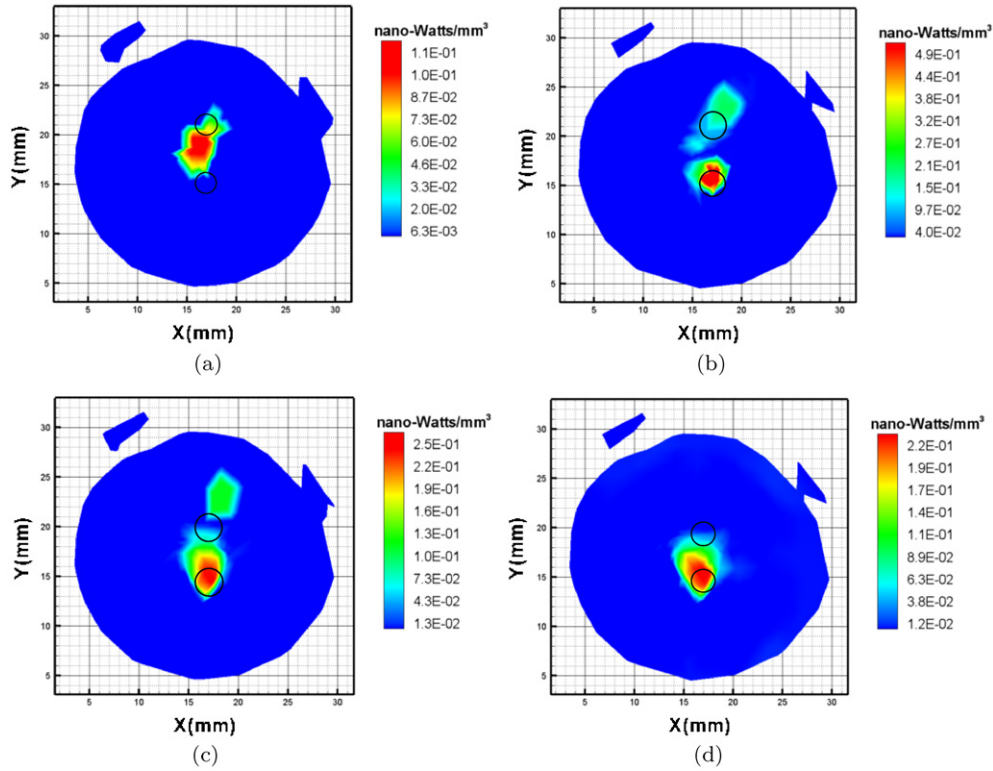


Figure 8. Spatial resolution evaluation of BLT reconstruction in view of adjustment to *a posteriori* permissible source region selection. (a) The reconstructed results with 4 mm edge-to-edge distance between two sources when the ratio factor $\gamma_{sp}^{(l)}$ is initially set to 10^{-4} ; (b)–(d) are the corresponding results when $\gamma_{sp}^{(l)}$ is initially set to 10^{-3} . The edge-to-edge distances between two sources are 4 mm, 3 mm and 2.75 mm, respectively. For the best display, the cross section is adjusted within ± 1 mm off the actual source's center.

3.4. Spatial resolution evaluation versus selection of permissible source region

As the source depth increases, more scattering will take place before the photons reach the surface of the small animal which is one of major difficulties in determining bioluminescent source distribution. It is especially difficult when two or more close sources exist in deep positions within the small animal body as an accurate accounting of the number of sources cannot be reconstructed even if the anatomical and multispectral information are used (Alexandrakis *et al* 2005). In this experiment, two spherical sources of equal intensity were placed on either side of the mouse phantom center with an edge-to-edge distance of 4 mm. They could not be resolved with the proposed tomographic method with a default parameter setting. The reconstructed results are shown in figure 8(a). However, when the selection factor $\gamma_{sp}^{(l)}$ was initially set to 10^{-3} , the two bioluminescent sources were distinguished via two mesh refinements even though the reconstructed source density had a large difference and the reconstructed position of one source had a slight offset, as shown in figure 8(b). In order to further verify the influence of the selection of permissible source region on the spatial resolution, we configured a set of experimental models with two sources which were placed on either side of the mouse phantom center and gradually approached each other. Figure 8(c) presents the reconstructed results with a 3 mm edge-to-edge distance between two sources.

Despite the fact that the reconstructed position of one source had a distinct offset, two sources could be resolved from the reconstructed results. However, no matter how the initial selection factor $\gamma_{sp}^{(l)}$ was adjusted in the tomographic algorithm, the BLT reconstruction could not resolve both sources in the 2.75 mm case. Figure 8(d) shows the reconstructed results with the same parameter setting as in the 3 mm case. From the above BLT reconstructions, it is clear that the selection of *a posteriori* permissible source region affects the spatial resolution capability of BLT to a large extent. Although *a posteriori* permissible source region selection is developed in this tomographic algorithm, a novel method is necessary to further explore the permissible source region.

4. Discussion and conclusion

In this paper, we have proposed a novel tomographic algorithm to reconstruct the bioluminescent source distribution. In the numerical verification, fast reconstruction speed, numerical robustness and stability of our tomographic algorithm are adequately explored in terms of deeper source reconstruction, optical property and geometric errors. Reconstruction comparisons between *a priori* and *a posteriori* permissible source region selections with single and multispectral measurements show the predominance of this algorithm. Even if the selection of *a posteriori* permissible source region needs to be adjusted, the acquisition of spatial resolution which cannot be obtained in the general case further confirms our algorithm's potential for BLT reconstruction. In addition, the algorithm can be properly evaluated by using the real mouse phantom and Monte Carlo-based synthetic data.

Compared with other molecular imaging modalities, bioluminescence imaging has played a pioneer role in preclinical studies because of the extensive application of bioluminescence in biology. As the transition from the verification experiment of simple phantoms to biological research using *in vivo* small animals is performed, the rapid increase of measured data sets and disposal of actual small animal models have brought big challenges to the reconstruction speed, quality, robustness and stability of the tomographic algorithm. The reconstructed results (figure 6) have shown that the whole region BLT reconstruction on the fixed discretized mesh is undesirable despite the fact that strong *a priori* information and a fine mesh are used, which is likely due to the severe ill-posedness of BLT. Multiscale reconstruction provides a graceful strategy for improving BLT reconstruction. The multigrid tomographic algorithm as a multiscale technique uses the coarse grid correction strategy to improve the quality of DOT reconstruction (Ye *et al* 2001). But the contradiction between the discretized scale choice of the used mesh and the computational burden for actual small animal reconstruction will be increasingly distinct with the use of uniform refined mesh and the initial reconstruction from the finest mesh. Whereas, the adaptive finite-element algorithm not only has the favorable coarse grid correction feature, but also improves reconstruction time and memory cost because the reconstruction strategy is based on the adaptive from-coarse-to-fine mesh sequence. Source reconstruction as a target localization of interest further benefits from *a posteriori* source space selection after the uniqueness problem is solved.

In the BLT prototype, employment of anatomical information and real-time optical properties allows for the imaging fusion of three different modalities, namely microCT/MRI, DOT and BLT. The high tolerance of optical property errors makes this algorithm more appropriate for the practical multimodality BLT system. Although a standard mouse phantom may be established beforehand for anatomical information through advanced dissection techniques or imaging modalities with high spatial resolution, as the basal *a priori* information for DOT and BLT reconstruction, the disposals of image volume, such as image segmentation, registration, volumetric mesh generation and so on, need to be further developed for improving

BLT reconstruction. The acquisition technique of near-infrared optical signals requires refinement in view of the complex surface geometry of small animals and noncontact detection (Ntziachristos *et al* 2005). In addition, the movement and breathing of *in vivo* small animals will likely produce an effect on BLT reconstruction because of the ill-posed nature. New methods need to be explored for dealing with these problems. In conclusion, many practical factors need further consideration for experimental BLT reconstruction. Our tomographic algorithm provides a significant imaging method and leads to high-performance BLT investigations in view of reconstruction quality, robustness, stability and speed.

Acknowledgments

We would like to thank the reviewers for their constructive suggestions. We gratefully thank Ying Liu, Melissa A Wade and Janet Webster for their extensive assistance and editorial refinement. We would also like to thank Dr William Paul Segars for providing the MOBY mouse phantom. This work is supported by Chair Professors of Cheung Kong Scholars Program, PCSIRT and CAS Hundred Talents Program. This work is also supported by NBRPC (2006CB705700), 863 Program (2006AA04Z216), NSTSP (2006BAH02A25), JRFOCYS (30528027), NSFC (30600151, 30500131 and 60532050) and BNSF (4051002, 4071003), China. Dr W X Cong and G Wang are supported in part by an NIH/NIBIB grant EB001685.

References

- Alexandrakis G, Rannou F R and Chatziioannou A F 2005 Tomographic bioluminescence imaging by use of a combined optical-PET (OPET) system: a computer simulation feasibility study *Phys. Med. Biol.* **50** 4225–41
- Alexandrakis G, Rannou F R and Chatziioannou A F 2006 Effect of optical property estimation accuracy on tomographic bioluminescence imaging: simulation of a combined optical-PET (OPET) system *Phys. Med. Biol.* **51** 2045–53
- Bhaumik S and Gambhir S S 2002 Optical imaging of renilla luciferase reporter gene expression in living mice *Proc. Natl Acad. Sci. USA* **99** 377–82
- Birgin E G and Martinez J M 2002 Large-scale active-set box-constrained optimization method with spectral projected gradients *Comput. Optim. Appl.* **23** 101–25
- Chaudhari A J, Darvas F, Bading J R, Moats R A, Conti P S, Smith D J, Cherry S R and Leahy R M 2005 Hyperspectral and multispectral bioluminescence optical tomography for small animal imaging *Phys. Med. Biol.* **50** 5421–41
- Cong W, Kumar D, Liu Y, Cong A and Wang G 2004 A practical method to determine the light source distribution in bioluminescent imaging *Developments in X-Ray Tomography IV* vol 5535 ed U Bonse (SPIE) pp 679–86
- Cong A, Liu Y, Kumar D, Cong W and Wang G 2005a Geometrical modeling using multiregional marching tetrahedra for bioluminescence tomography *Medical Imaging 2005: Visualization, Image-Guided Procedures, and Display* vol 5744 ed K R Cleary and R L Galloway Jr pp 756–63
- Cong A X and Wang G 2006 Multispectral bioluminescence tomography: methodology and simulation *Int. J. Biomed. Imaging* **2006** 1–7
- Cong W *et al* 2005b Practical reconstruction method for bioluminescence tomography *Opt. Express* **13** 6756–71
- Contag C H and Bachmann M H 2002 Advances in bioluminescence imaging of gene expression *Annu. Rev. Biomed. Eng.* **4** 235–60
- Coquoz O, Troy T L, Jekic-McMullen D and Rice B W 2003 Determination of depth of *in vivo* bioluminescent signals using spectral imaging techniques *Genetically Engineered and Optical Probes for Biomedical Applications Proc. SPIE* **4967** 37–45
- Dehghani H, Davis S C, Jiang S, Pogue B W, Paulsen K D and Patterson M S 2006 Spectrally resolved bioluminescence optical tomography *Opt. Lett.* **31** 365–7
- Diniz-Ehrhardt M A, Gomes-Ruggiero M A and Santos S A 1997 Comparing the numerical performance of two trust-region algorithms for large-scale bound-constrained minimization *Revista Latino Am. Invest. Operat.* **7** 23–54
- Gibson A P, Hebden J C and Arridge S R 2005 Recent advances in diffuse optical imaging *Phys. Med. Biol.* **50** R1–43
- Hanke M and Hansen P C 1993 Regularization methods for large-scale problems *Surv. Math. Ind.* **3** 253–315

- Hansen P C 1999 *Rank-Deficient and Discrete Ill-Posed Problems: Numerical Aspects of Linear Inversion* (Philadelphia, PA: Society for Industrial and Applied Mathematics)
- Joshi A, Bangerth W and Sevick-Muraca E M 2004 Adaptive finite element based tomography for fluorescence optical imaging in tissue *Opt. Express* **12** 5402–17
- Kuo C, Coquoz O, Stearns D G and Rice B W 2004 Diffuse luminescence imaging tomography of *in vivo* bioluminescent markers using multi-spectral data *Society for Molecular Imaging 3rd Annual Meeting (St Louis)* vol 3 (Cambridge, MA: MIT Press) p 227
- Li H, Tian J, Zhu F, Cong W, Wang L V, Hoffman E A and Wang G 2004 A mouse optical simulation environment (MOSE) to investigate bioluminescent phenomena in the living mouse with the Monte Carlo method *Acad. Radiol.* **11** 1029–38
- Lorensen W E and Cline H E 1987 Marching cubes: a high resolution 3D surface construction algorithm *Proc. 14th Annual Conf. on Computer Graphics and Interactive Techniques* vol 21, pp 163–9
- Lv Y, Tian J, Cong W, Wang G, Luo J, Yang W and Li H 2006 A multilevel adaptive finite element algorithm for bioluminescence tomography *Opt. Express* **14** 8211–23
- Massoud T F and Gambhir S S 2003 Molecular imaging in living subjects: seeing fundamental biological processes in a new light *Genes Dev.* **17** 545–80
- Ntziachristos V, Hielscher A H, Yodh A G and Chance B 2001 Diffuse optical tomography of highly heterogeneous media *IEEE Trans. Med. Imaging* **20** 470–8
- Ntziachristos V, Ripoll J, Wang L V and Weissleder R 2005 Looking and listening to light: the evolution of whole body photonic imaging *Nat. Biotechnol.* **23** 313–20
- Pogue B W, McBride T O, Osterberg U L and Paulsen K D 1999 Comparison of imaging geometries for diffuse optical tomography of tissue *Opt. Express* **4** 270–86
- Ripoll J, Nieto-Vesperinas M, Weissleder R and Ntziachristos V 2002 Fast analytical approximation for arbitrary geometries in diffuse optical tomography *Opt. Lett.* **27** 527–9
- Ripoll J, Schulz R B and Ntziachristos V 2003 Free-space propagation of diffuse light: theory and experiments *Phys. Rev. Lett.* **91** 103901–4
- Roy R and Sevick-Muraca E M 2000 Active constrained truncated Newton method for simple-bound optical tomography *J. Opt. Soc. Am. A* **17** 1627–41
- Segars W P, Tsui B M W, Frey E C, Johnson G A and Berr S S 2004 Development of a 4D digital mouse phantom for molecular imaging research *Mol. Imaging Biol.* **6** 149–59
- Wang G, Hoffman E A, McLennan G, Wang L V, Suter M and Meinel J F 2003 Development of the first bioluminescence CT scanner *Radiology* **566** 229
- Wang G, Li Y and Jiang M 2004 Uniqueness theorems in bioluminescence tomography *Med. Phys.* **31** 2289–99
- Wu Z 2001 Accurate and efficient three-dimensional mesh generation for biomedical engineering applications *PhD Thesis* Worcester Polytechnic Institute
- Wu Z and Sullivan J M Jr 2003 Multiple material marching cubes algorithm *Int. J. Numer. Methods Eng.* **58** 189–207
- Ye J C, Bouman C A, Webb K J and Millane R P 2001 Nonlinear multigrid algorithms for Bayesian optical diffusion tomography *IEEE Trans. Image Process.* **10** 909–22
- Zhao H, Doyle T C, Coquoz O, Kalish F, Rice B W and Contag C H 2005 Emission spectra of bioluminescent reporters and interaction with mammalian tissue determine the sensitivity of detection *in vivo* *J. Biomed. Opt.* **10** 041210–1